(Received 7 May 2025, Accepted 12 June 2025, Scheduled 27 June 2025)

Modelling and Analysis of Magnetic Field Distribution Generated by a Magnetised Paraboloid

Van Tai Nguyen[1,*] and Thi Phuoc Van Nguyen[2]

[1] *Electrical-Electronic Engineering Technology, Thanh Do University, Hanoi, Vietnam*
[2] *Information Technology, Thanh Do University, Hanoi, Vietnam, ntpvan@thanhdouni.edu.vn*

ABSTRACT: Permanent magnets have a unique ability to generate a permanent magnetic field that has been found in various applications. In this study, to facilitate the design and optimization processes of magnetic devices, fast-computed expressions of the magnetic field created by a magnetised paraboloid are developed. It is demonstrated that the derived models are in good agreement with the conventional Finite Element Analysis (FEA). Moreover, these models are multiple magnitudes faster than the FEA in terms of computational time. Furthermore, analysing the magnetic field distribution generated by this magnet, it is shown that the field is concentrated around its revolute axis. In addition, the field is sharply concentrated and pointy, close to the apex of the paraboloid. The field expressions and their properties are expected to assist in the design and optimization processes of magnetic devices utilizing this magnet, such as in static magnetic field brain stimulation.

1. INTRODUCTION

With the unique ability to produce permanent magnetic flux into airspace, permanent magnets have been utilised in many devices ranging from robotics to medical applications [1, 2]. For example, permanent magnets have been applied in renewable energy to harvest energy from motion [3]. A static magnetic field generated by permanent magnets can be applied in transcranial static magnetic field stimulation as a noninvasive method to treat brain diseases and movement disorders [4–6]. To facilitate the design and optimization processes of permanent magnetic devices, it is important to have fast-computed magnetic field models generated by permanent magnets. Moreover, understanding the magnetic field distribution of those magnets can aid in the utilization of these materials. Furthermore, the conventional method, such as Finite Element Analysis, which has been used to analyse the magnetic field created by permanent and electric magnets, can be time-consuming [2] for design and optimization purposes. This demand has led to numerous attempts to develop fast-computed expressions and analyse the magnetic fields of permanent magnets of different types. In addition, due to the superposition principle, the magnetic field of a composite shape can be calculated by summing the magnetic fields generated by permanent magnets of basic shapes, which can be determined by decomposing the composite-shaped magnet [2]. Therefore, the magnetic fields created by permanent magnets of basic shapes such as cylinders, elliptical cylinders, cones, and rectangular bars, which have been found in research and real-world applications, have been expressed and studied [2, 7–11]. To develop reliable magnetic field equations for parametric studies, Hart et al. developed efficient analytical expressions of the magnetic field generated by an axially magnetised and conically shaped permanent magnet [7]. Nguyen and Lu [8] developed exact analytical expressions of the magnetic field created by a cylindrical magnet with diametrical magnetization. These authors also derived efficient models of the field of an elliptical cylinder permanent magnets [9]. Yan et al. analysed the field distribution of a permanent magnet spherical actuator [11] in the development of the novel three-degree-of-freedom actuator. Moreover, the external fields generated by ellipsoids and spheroids with uniform magnetization have been expressed and studied [10]. Within basic geometrical shapes, a paraboloid is a quadratic surface with one axis of symmetry. This shape is special due to its pointy apex, which can potentially yield a concentrated magnetic field. However, the magnetic field distribution of a permanent magnet in the shape of a paraboloid has not been studied, and fast-computed expressions of this field have not been developed. Therefore, this study aims to develop efficient expressions of the magnetic field of a magnetised paraboloid and provide an understanding of the field distribution of this magnet. The results of this study are expected to inspire further research and development of magnetic devices using parabolic permanent magnets. These magnets can be an alternative source of static magnetic fields, alongside other types such as conventional cylindrical permanent magnets used in non-invasive brain stimulation [4–6, 12]. The knowledge of the field distribution of these magnets, along with efficient expressions for the field, can facilitate the design and optimization processes of such magnetic devices.

The rest of this article is organised as follows. Section 2 models the magnetic field generated by a magnetised paraboloid. The validation of these models is presented in Section 3. Section 4 provides an analysis of the magnetic field distribution. A brief discussion and conclusion are drawn in Section 5.

* Corresponding author: Van Tai Nguyen (nvtai@thanhdouni.edu.vn).

2. MODELLING OF THE MAGNETIC FIELD OF A PARABOLOID

The magnetic field distribution created by a permanent magnet can be computed based on the charge model [2] as follows:

$$\vec{H} = \frac{1}{4\pi\mu_0} \oiint_s \frac{\sigma_m \overrightarrow{SP}}{\left\|\overrightarrow{SP}\right\|_2^3} ds + \frac{1}{4\pi\mu_0} \iiint_v \frac{\rho_m \overrightarrow{SP}}{\left\|\overrightarrow{SP}\right\|_2^3} dv, \quad (1)$$

where S is a source point from the paraboloid; P is the computed point (Fig. 1); σ_m (A/m) and ρ_m (A/m^2) are the surface and volume charge densities, respectively.

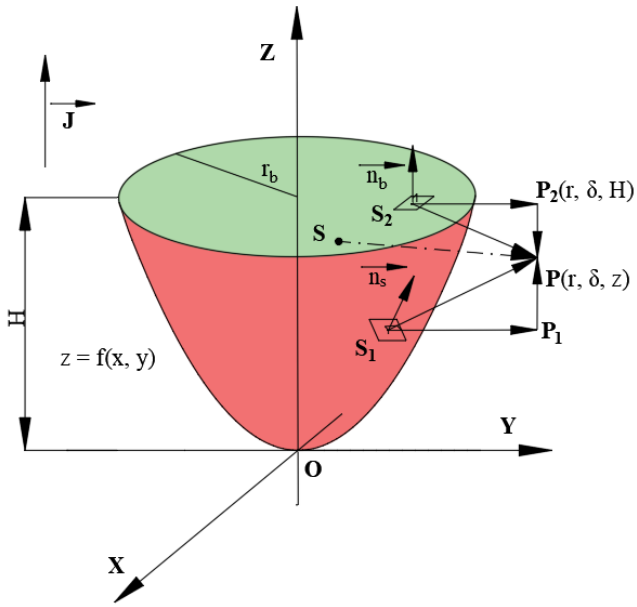

FIGURE 1. 3D geometry of a paraboloid.

Due to the uniformity of the magnetization vector, the volume charge density, which is calculated as the divergence of this vector, is equal to zero. $\rho_m = -\nabla \cdot \vec{J} = 0$. The surface charge density can be determined as $\sigma_m = \vec{J} \cdot \vec{n}$, with $\vec{n}$ being the outward unit vector normal to the magnet's surface. Therefore, Eq. (1) is reduced to Eq. (2), with only the surface component contributing to the magnetic field.

$$\begin{aligned} \vec{H} &= \frac{1}{4\pi\mu_0} \oiint_{s_1} \frac{\left(\vec{J} \cdot \vec{n_s}\right) \overrightarrow{S_1P}}{\left\|\overrightarrow{S_1P}\right\|_2^3} ds_1 \\ &+ \frac{1}{4\pi\mu_0} \oiint_{s_2} \frac{\left(\vec{J} \cdot \vec{n_b}\right) \overrightarrow{S_2P}}{\left\|\overrightarrow{S_2P}\right\|_2^3} ds_2, \end{aligned} \quad (2)$$

where S_1 and S_2 are the source points from the lateral and base surfaces of the magnet (Fig. 1), respectively; $\vec{n_s}$ and $\vec{n_b}$ are the unit vectors normal to the lateral and base surfaces of the magnet.

The base charge density

$$\vec{J} \cdot \vec{n_b} = J, \quad (3)$$

and the lateral surface charge density $\vec{J} \cdot \vec{n_s}$ can be expressed as follows:

$$\begin{aligned} \vec{J} \cdot \vec{n_s} &= \frac{\vec{J} \cdot \nabla g}{\|\nabla g\|} = \frac{\vec{J} \cdot \left(\frac{\partial f}{\partial x}\vec{u_x} + \frac{\partial f}{\partial y}\vec{u_y} - 1\vec{u_z}\right)}{\sqrt{\left(\frac{\partial f}{\partial x}\right)^2 + \left(\frac{\partial f}{\partial y}\right)^2 + 1}} \\ &= \frac{-J}{\sqrt{\left(\frac{\partial f}{\partial x}\right)^2 + \left(\frac{\partial f}{\partial y}\right)^2 + 1}}, \end{aligned} \quad (4)$$

where function $g(x, y, z) = z - f(x, y)$, and $\vec{u_x}$, $\vec{u_y}$, and $\vec{u_z}$ are the unit vectors of the $OXYZ$.

For the circular paraboloid $z = f(x, y) = a\left(x^2 + y^2\right)$, it is worth noting that due to the arrangement between the paraboloid and Cartesian coordinate system (Fig. 1), the coefficient $a > 0$, and Eq. (4) can be derived as follows.

$$\vec{J} \cdot \vec{n_s} = \frac{-J}{\sqrt{4a^2x^2 + 4a^2y^2 + 1}}, \quad (5)$$

In a cylindrical coordinate system (r, θ, z) with the azimuthal angle θ starting from the axis OX and the radial distance r, at any given point (r_1, θ, z_1) Eq. (5) can be rewritten as follows:

$$\begin{aligned} \vec{J} \cdot \vec{n_s} &= \frac{-J}{\sqrt{4a^2\left(r_1 \cos\theta\right)^2 + 4a^2\left(r_1 \sin\theta\right)^2 + 1}} \\ &= \frac{-J}{\sqrt{4a^2r_1^2 + 1}}, \end{aligned} \quad (6)$$

The infinitesimal areas ds_1 and ds_2 can be computed in the cylindrical coordinate system below:

$$ds_1 = \sqrt{4a^2r_1^2 + 1} r_1 d\theta dr_1, \quad (7)$$

$$ds_2 = r_2 dr_2 d\theta, \quad (8)$$

Vector $\overrightarrow{S_1P}$ can be projected onto the three axes of the cylindrical coordinate system based on Fig. 1 and Fig. 2(a) as follows:

$$\begin{aligned} \overrightarrow{S_1P} &= \overrightarrow{S_1S_1'} + \overrightarrow{S_1'P_1} + \overrightarrow{P_1P} = r_1 \sin\left(\delta - \theta\right) \vec{u_\theta} \\ &+ \left(r - r_1 \cos\left(\delta - \theta\right)\right) \vec{u_r} + \left(z - z_1\right) \vec{u_z}, \end{aligned} \quad (9)$$

Vector $\overrightarrow{S_2P}$ can also be rewritten as follows:

$$\begin{aligned} \overrightarrow{S_2P} &= \overrightarrow{S_2S_2'} + \overrightarrow{S_2'P_2} + \overrightarrow{P_2P} = r_2 \sin\left(\delta - \theta\right) \vec{u_\theta} \\ &+ \left(r - r_2 \cos\left(\delta - \theta\right)\right) \vec{u_r} + \left(z - H\right) \vec{u_z}, \end{aligned} \quad (10)$$

Inserting Eqs. (3), (6)–(10) into Eq. (2) with a note that the base radius $r_b = \sqrt{H/a}$ and $z_1 = ar_1^2$, the magnetic field components can be expressed as follows:

The axial component:

H_{Axial}

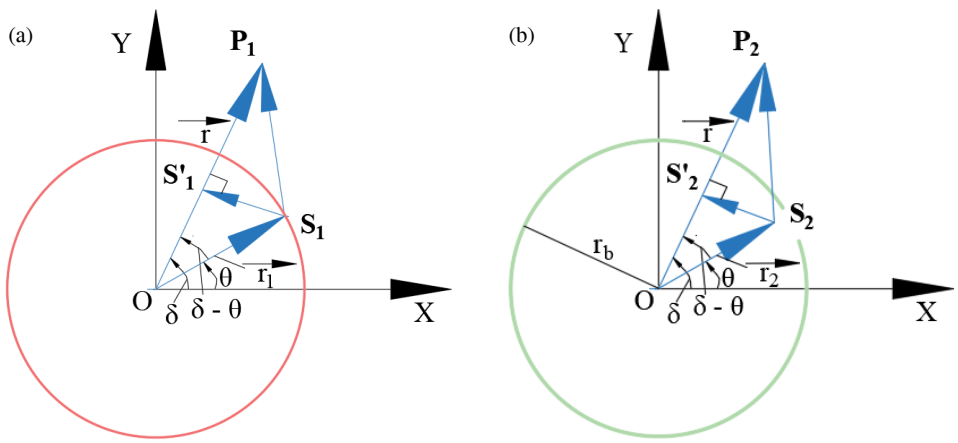

FIGURE 2. Projections on OXY plane: (a) Projection from the base surface and (b) Projection from the lateral surface.

$$=\frac{J}{4\pi\mu_0}\int_0^{2\pi}\int_0^{\sqrt{H/a}}\frac{-\left(z-ar_1^2\right)r_1}{\left(r_1^2+r^2-2r_1r\cos\left(\delta-\theta\right)+\left(z-ar_1^2\right)^2\right)^{3/2}}dr_1d\theta$$

$$+\frac{J}{4\pi\mu_0}\int_0^{2\pi}\int_0^{\sqrt{H/a}}\frac{\left(z-H\right)r_2}{\left(r_2^2+r^2-2r_2r\cos\left(\delta-\theta\right)+\left(z-H\right)^2\right)^{3/2}}dr_2d\theta, \quad (11)$$

The azimuthal component:

$$H_{Azimuthal}$$

$$=\frac{J}{4\pi\mu_0}\int_0^{2\pi}\int_0^{\sqrt{H/a}}\frac{-\sin\left(\delta-\theta\right)r_1^2}{\left(r_1^2+r^2-2r_1r\cos\left(\delta-\theta\right)+\left(z-ar_1^2\right)^2\right)^{3/2}}dr_1d\theta$$

$$+\frac{J}{4\pi\mu_0}\int_0^{2\pi}\int_0^{\sqrt{H/a}}\frac{\sin\left(\delta-\theta\right)r_1^2}{\left(r_2^2+r^2-2r_2r\cos\left(\delta-\theta\right)+\left(z-H\right)^2\right)^{3/2}}dr_2d\theta$$

$$=0, \quad (12)$$

It can be evaluated from Eq. (12) that the azimuthal component is equal to zero due to the integral of the odd functions.

The radial component:

$$H_{Radial}$$

$$=\frac{J}{4\pi\mu_0}\int_0^{2\pi}\int_0^{\sqrt{H/a}}\frac{-\left(r-r_1cos\left(\delta-\theta\right)\right)r_1}{\left(r_1^2+r^2-2r_1r\cos\left(\delta-\theta\right)+\left(z-ar_1^2\right)^2\right)^{3/2}}dr_1d\theta$$

$$+\frac{J}{4\pi\mu_0}\int_0^{2\pi}\int_0^{\sqrt{H/a}}\frac{\left(r-r_2\cos\left(\delta-\theta\right)\right)r_2}{\left(r_2^2+r^2-2r_2r\cos\left(\delta-\theta\right)+\left(z-H\right)^2\right)^{3/2}}dr_2d\theta, \quad (13)$$

It is worth noting that the magnetic flux density $\vec{B}$ can be determined knowing the magnetic field intensity $\vec{H}$ using Eqs. (14) and (15) as follows:

$$\vec{B} = \mu_0\vec{H}, \text{ in the air space,} \quad (14)$$

$$\vec{B} = \mu_0\vec{H}+\vec{J}, \text{ inside the magnet} \quad (15)$$

3. SEMI-ANALYTICAL MODEL VERIFICATION

In this section, the semi-analytical model is validated against the Finite Element (FE) Analysis which is carried out using the commercial software electromagnetic simulation software (EMS) from EMWORKS® integrated in 3D INVENTOR®. The permanent magnet used in this simulation has a height of 0.0128 m with the axial magnetization $J = 1$ T, the coefficient of the parabolic profile $a = 0.2$, the axial coordinate $z = 0.015$ m, the azimuthal angle $\alpha = \pi/6$, and the plot is within the range $r = [0, 0.030]$ m. In the FE simulation, the magnet is surrounded by a small air region which lies in a bigger air region. This division of the air areas enables the assignment of fine mesh to the magnet and small air and coarser mesh to the big air to save computational expenses. As a result, there are 1,397,125 nodes and 8,251,774 elements for the simulation convergence using the EMS. Python programming language [13] was used in this experiment to execute the semi-analytical models. It is worth noting that, in this study, sequential programming [14] is utilised. Parallel programming in Python and the use of other programming languages such as C [15] and C++ [16] can be applied to accelerate the computation [17]; however, this is not within the focus of this study. The results shown in Fig. 3 demonstrate the excellent agreement between the semi-analytical and FE models. Moreover, Table 1 provides some examples of randomly extracted points along the radial axis. It reinforces that the computed fields from the two methods are in excellent agreement. The minimum, maximum, and average errors between the two methods are 0.026%, 0.991%, and 0.425% for the axial component, and 0.032%, 1.295%, and 0.517% for the radial component, respectively. The azimuthal component computed using the FE fluctuates around zero and is considered noise in the FE simulation.

The computational time of the semi-analytical model is significantly lower than that of the FE method. For a set of geometrical and material parameters of a magnetised paraboloid, it took an average of 0.0112 seconds and 0.0116 seconds to compute the axial and radial components, respectively (Table 2); 3000 random samples were utilised in this experiment. On the other hand, the FE method took an average of 300 seconds to complete the simulation for a set of geometrical and material

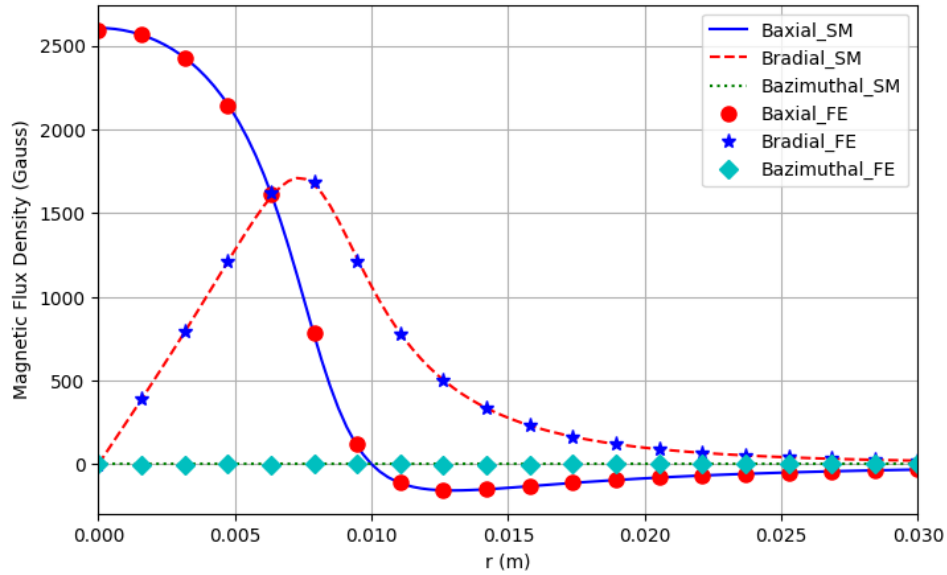

FIGURE 3. Verification of the semi-analytical model against the Finite Element (FE) method: B_axial (azimuthal, radial)_SE and B_axial (azimuthal, radial)_FE denote the magnetic flux density of the axial (azimuthal, radial) components computed using the semi-analytical and FE models, respectively; the height of the magnet is 0.0128 m with the magnetization $J = 1$ T, the coefficient $a = 0.2$, the axial coordinate $z = 0.015$ m, the azimuthal angle $\alpha = \pi/6$, and the plot is within the range $r = [0, 0.030]$ m.

TABLE 1. Field comparison at randomly extracted points along the radial axis.

r (m)	Baxial_SM (Gauss*)	Baxial_FE (Gauss)	Bradial_SM (Gauss)	Bradial_FE (Gauss)	Bazimuthal_SM (Gauss)	Bazimuthal_FE (Gauss)
0.001212	2581.817	2581.136	297.245	297.967	0.000	2.872
0.003636	2362.935	2359.746	915.579	919.595	0.000	6.399
0.005152	2041.312	2026.724	1319.875	1310.433	0.000	4.418
0.005758	1839.242	1845.731	1473.478	1492.803	0.000	−1.728
0.006061	1729.127	1721.468	1543.468	1558.893	0.000	−3.699
0.008485	467.237	464.516	1544.451	1533.994	0.000	−0.612
0.014545	−145.407	−145.617	309.601	308.426	0.000	0.204
0.016667	−119.585	−118.411	191.615	191.676	0.000	−0.340
0.019091	−92.295	−91.891	117.671	117.323	0.000	0.052
0.026061	−44.876	−44.693	37.332	37.298	0.000	0.080
Min error (%)	0.026		0.032		N/A	N/A
Max error (%)	0.991		1.295		N/A	N/A
Average error (%)	0.425		0.517		N/A	N/A

*1 Gauss $= 10^{-4}$ Tesla (T)

parameters of the magnet. It is worth noting that the time comparison between these models was conducted on the same personal computer with a processor Intel(R) Core(TM) i5-8250U CPU @ 1.60 GHz 1.80 GHz.

4. MAGNETIC FIELD ANALYSIS

To analyse the magnetic field distribution of an axially magnetised paraboloid with various coefficients a, Figs. 4 and 5 depict the axial and radial components of the magnet. The parameters of the permanent magnet and coordinates of measuring points in

TABLE 2. Execution time.

Field components	Semi-analytical model (seconds)	Finite Element Method (seconds)
Axial component	0.0112	300
Radial component	0.0116	300

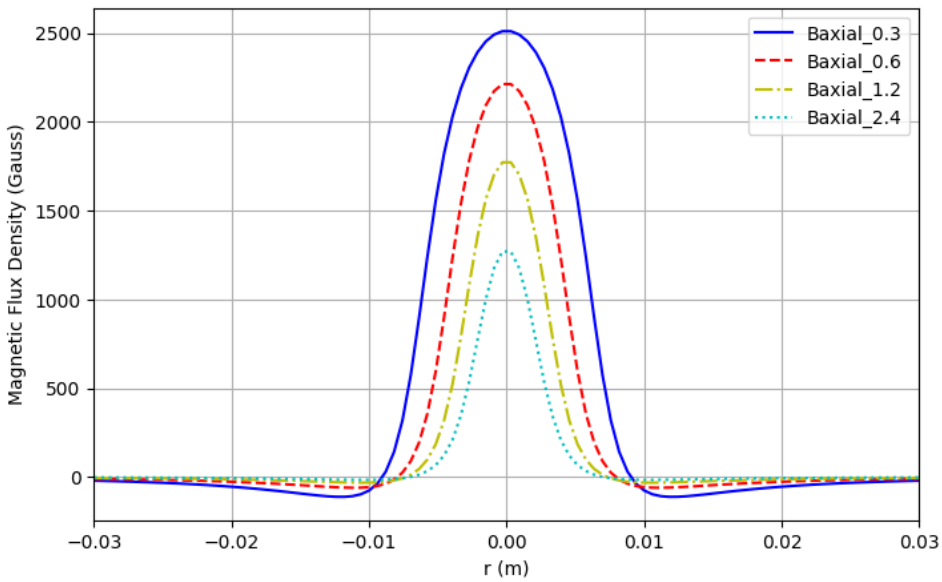

FIGURE 4. Magnetic field distribution according to various coefficients a: Axial component. Parameters of the permanent magnet and coordinates of measuring points are $J = 1$ Tesla, $H = 0.0128$ m, $z = 0.015$ m, $r = [-0.03\,\text{m}, 0.03\,\text{m}]$. Baxial_0.3, Baxial_0.6, Baxial_1.2, Baxial_2.4 — Magnetic flux density with coefficient a equal to 0.3, 0.6, 1.2, and 2.4, respectively.

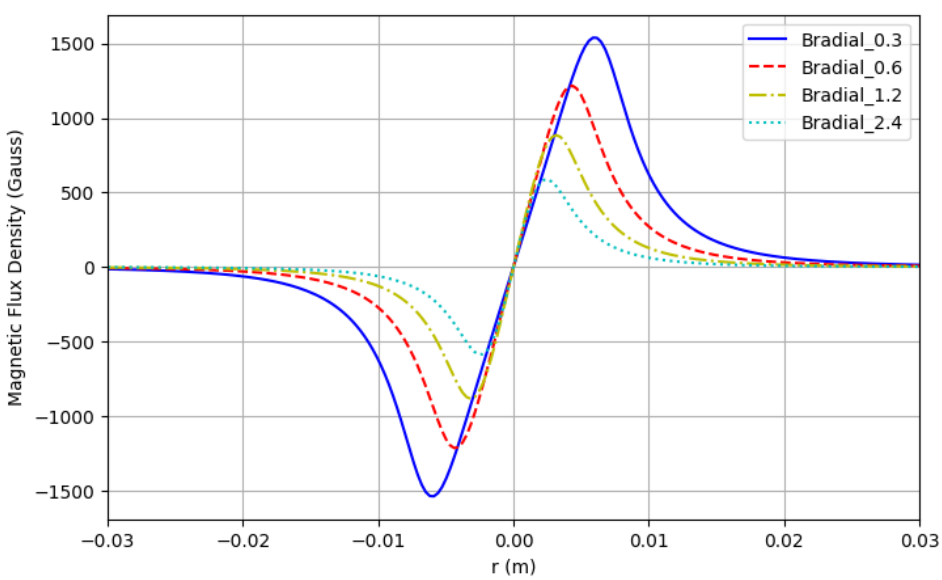

FIGURE 5. Magnetic field distribution according to various coefficients a: Radial component. Parameters of the permanent magnet and coordinates of measuring points are $J = 1$ Tesla, $H = 0.0128$ m, $z = 0.015$ m, $r = [-0.03\,\text{m}, 0.03\,\text{m}]$. Bradial_0.3, Bradial_0.6, Bradial_1.2, Bradial_2.4 — Magnetic flux density with coefficient a equal to 0.3, 0.6, 1.2, and 2.4, respectively.

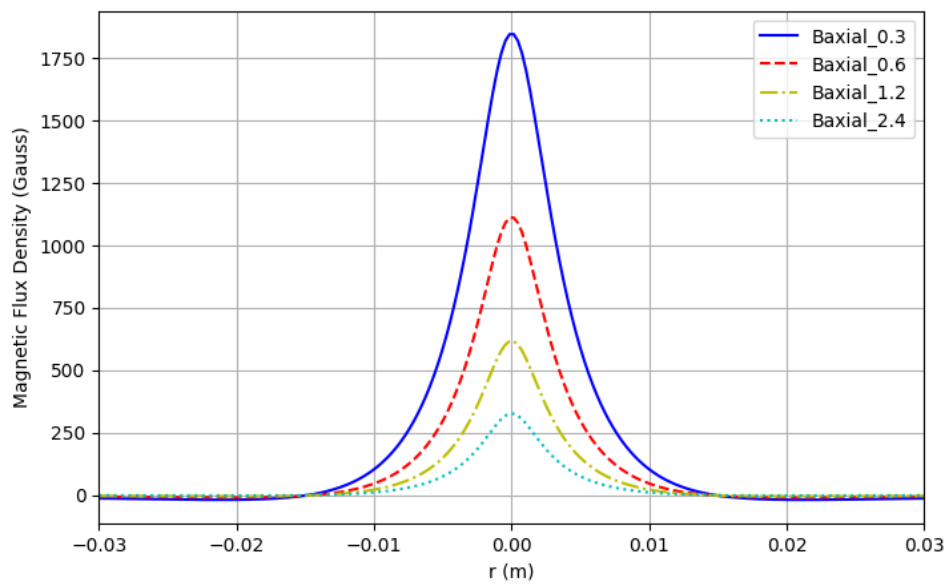

FIGURE 6. Magnetic field distribution according to various coefficients a: Axial component. Parameters of the permanent magnet and coordinates of measuring points are $J = 1$ Tesla, $H = 0.0128$ m, $z = -0.0022$ m, $r = [-0.03$ m, 0.03 m]. Baxial_0.3, Baxial_0.6, Baxial_1.2, Baxial_2.4 — Magnetic flux density with coefficient a equal to 0.3, 0.6, 1.2, and 2.4, respectively.

a cylindrical coordinate system (Figs. 1 and 2) are implemented as the magnetization $J = 1$ Tesla; the height $H = 0.0128$ m; z coordinate is 0.015 m (0.0022 m above the base); radial coordinates are in the range $[-0.03$ m, 0.03 m]; the coefficient a is equal to 0.3, 0.6, 1.2, and 2.4. Fig. 4 shows that with the increase of the coefficient a, the magnitude of the axial component of the field decreases. This is valid for the maximum values of the magnitude as well (Table 3), with the maximum magnitudes for the axial component 2511.898 (Gauss) and 1281.468 (Gauss) for the coefficient equal to 0.3 and 2.4, respectively. Moreover, the field reaches the maximum magnitude at points lying on the revolute axis of the paraboloid (when radial distance $r = 0$ m). On the other hand, Fig. 5 demonstrates that the radial component of the field is equal to zero at points lying on the revolute axis. Then, the magnitude of this component increases to reach the maximum before decreasing. Similar to the axial component, the maximum magnitudes of the radial component decrease from 1533.278 (Gauss) to 579.918 (Gauss) when the coefficient increases from 0.3 to 2.4 (Table 3), respectively.

Figures 6 and 7 plot the magnetic field distribution along a radial distance with $z = -0.0022$ m below the apex of the paraboloid (origin O of the OXYZ coordinate system in Fig. 1). The other parameters and coordinates of measuring points are the same as above ($z = 0.015$ m). It is shown that the axial component is concentrated around the revolute axis of the paraboloid and reaches maximum along this axis (when radial distance equals zero). The magnitude of the field decreases with the increase of the coefficient a. The maximum magnitude decreases from 1847.806 Gauss to 325.688 Gauss when the coefficient a is reduced from 0.3 to 2.4, respectively (Table 4). Fig. 7 demonstrates that the radial component of the field equals zero at the revolute axis (the radial distance is zero). The magnitude of the field increases with the increase of the radial distance to reach the maximum before nonlinearly decreasing. The maximum magnitudes of the radial component decrease from 698.100 Gauss to 119.640 Gauss when the coefficient decreases from 0.3 to 2.4 (Table 4).

To provide more insights into the field distribution when the coefficient a is constant, and the height of the magnet H is changing, Figs. 8 and 9 depict the axial and component of the magnetic flux density generated from an axially magnetised paraboloid. The parameters of the permanent magnet and coordinates of measuring points are $J = 1$ Tesla, $a = 0.3$, $z = 0.015$ m, $r = [-0.03$ m, 0.03 m]; the height H equals 0.009 m, 0.0128 m, 0.013 m, and 0.014 m. Fig. 8 shows that the axial component of the field is concentrated around the revolute axis of the magnet and reaches maximum magnitude along this axis. Moreover, in contrast to the case when the height is constant, and the coefficient changes, the maximum magnitude increases when the height increases. This plot's maximum magnitude increases from 732.492 Gauss to 3334.499 Gauss when the height increases from 0.009 m to 0.014 m (Table 5). However, Fig. 9 demonstrates that the radial component of the field is reduced to zero along the revolute axis. The magnitude of this component increases to reach the maximum values before decreasing nonlinearly when the radial distance increases. The maximum magnitudes of this component increase from 339.489 Gauss to 2655.404 Gauss when the height increases from 0.009 m to 0.014 m (Table 5).

In addition, the magnetic field distribution along the radial distance with $z = -0.0022$ m below the apex point of the paraboloid is plotted in Figs. 10 and 11. It is shown that the axial component is concentrated around and reaches the maximum values at the revolute axis and is pointier than the field above the base, as discussed above. The maximum magnitudes

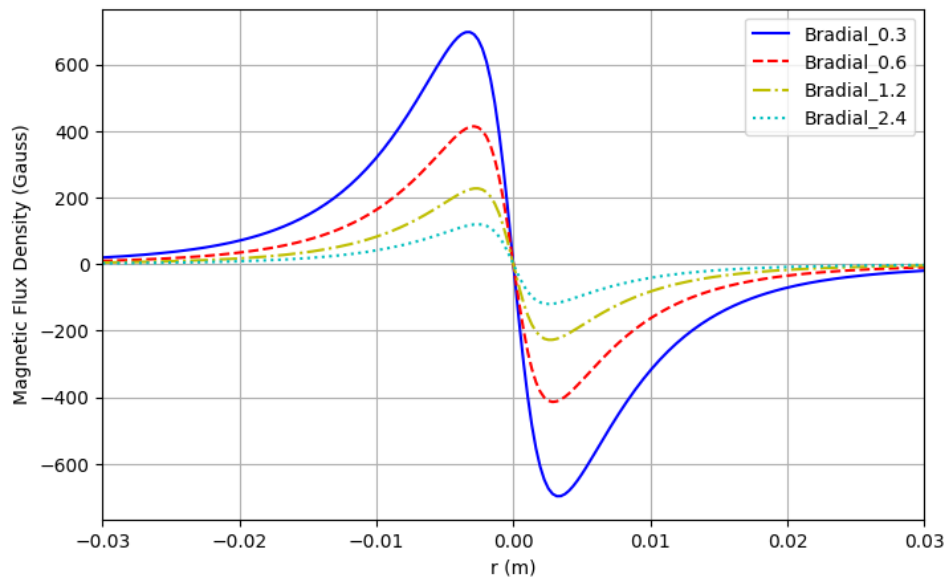

FIGURE 7. Magnetic field distribution according to various coefficients a: Radial component. Parameters of the permanent magnet and coordinates of measuring points are $J = 1$ Tesla, $H = 0.0128$ m, $z = -0.0022$ m, $r = [-0.03$ m, 0.03 m]. Bradial_0.3, Bradial_0.6, Bradial_1.2, Bradial_2.4 — Magnetic flux density with a coefficient equal to 0.3, 0.6, 1.2, and 2.4, respectively.

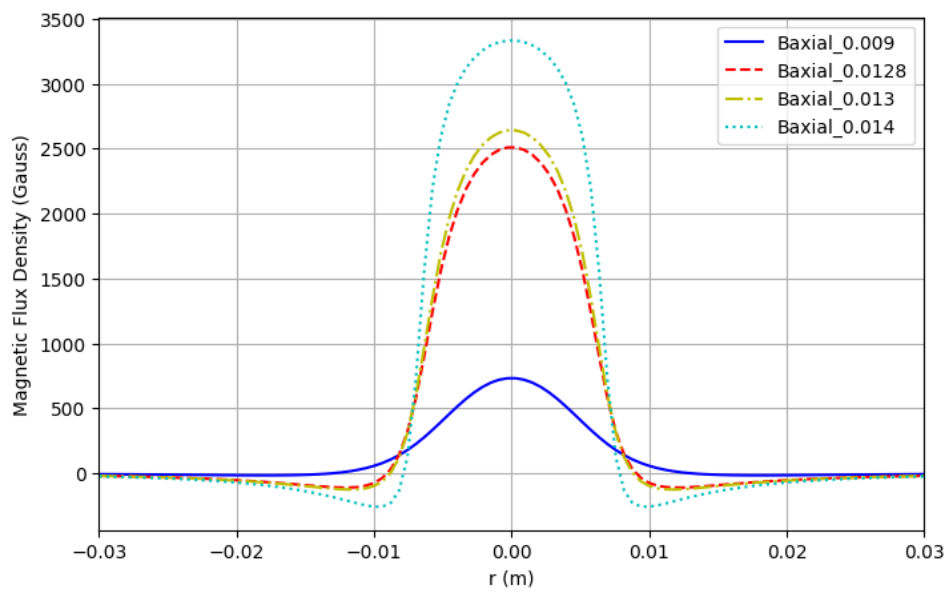

FIGURE 8. Magnetic field distribution according to various heights H: Axial component. Parameters of the permanent magnet and coordinates of measuring points are $J = 1$ Tesla, $a = 0.3$, $z = 0.015$ m, $r = [-0.03$ m, 0.03 m]. Bradial_0.009, Bradial_0.0128, Bradial_0.013, Bradial_0.014 — Magnetic flux density with the height H equal to 0.009 m, 0.0128 m, 0.013 m, and 0.014 m, respectively.

TABLE 3. Peak values ($z = 0.015$ m).

a	Axial component (Gauss)	Radial component (Gauss)
0.3	2511.898	1533.278
0.6	2216.457	1208.446
1.2	1779.859	880.969
2.4	1281.468	579.918

TABLE 4. Peak values ($z = -0.0022$ m).

a	Axial component (Gauss)	Radial component (Gauss)
0.3	1847.806	698.100
0.6	1112.485	413.387
1.2	616.716	227.792
2.4	325.688	119.640

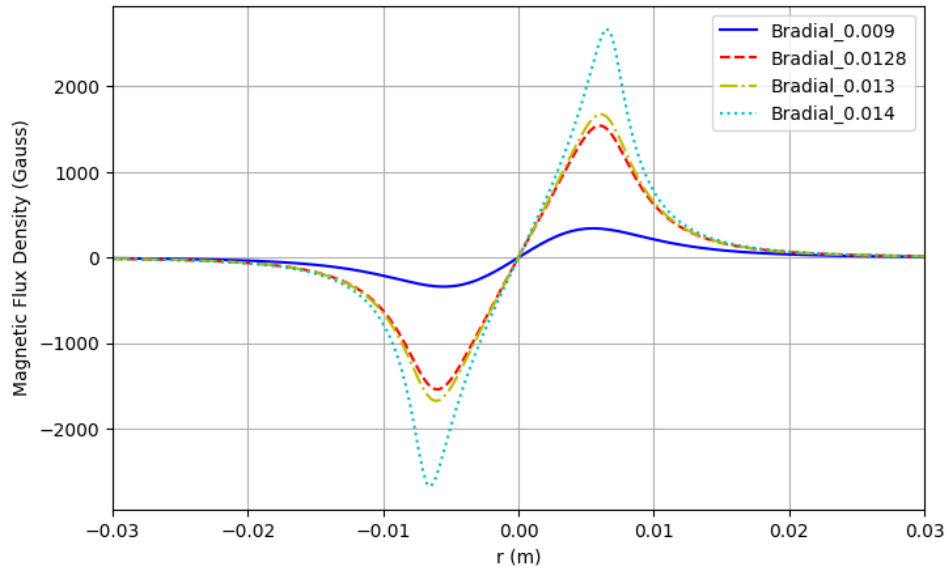

FIGURE 9. Magnetic field distribution according to various heights H: Radial component. Parameters of the permanent magnet and coordinates of measuring points are $J = 1$ Tesla, $a = 0.3$, $z = 0.015$ m, $r = [-0.03\,\text{m}, 0.03\,\text{m}]$. Bradial_0.009, Bradial_0.0128, Bradial_0.013, Bradial_0.014 — Magnetic flux density with the height H equal to 0.009 m, 0.0128 m, 0.013 m, and 0.014 m, respectively.

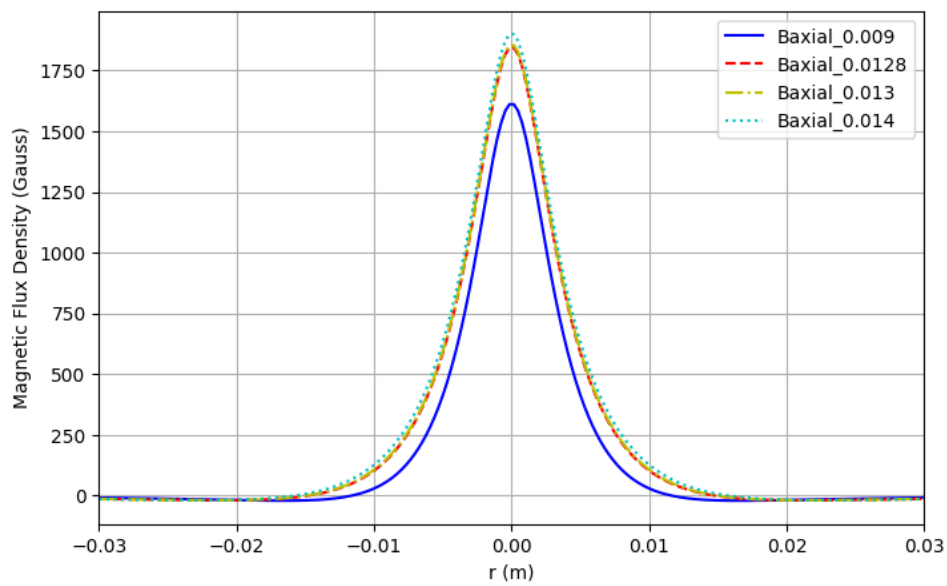

FIGURE 10. Magnetic field distribution according to various heights H: Axial component. Parameters of the permanent magnet and coordinates of measuring points are $J = 1$ Tesla, $a = 0.3$, $z = -0.0022$ m, $r = [-0.03\,\text{m}, 0.03\,\text{m}]$. Bradial_0.009, Bradial_0.0128, Bradial_0.013, Bradial_0.014 — Magnetic flux density with the height H equal to 0.009 m, 0.0128 m, 0.013 m, and 0.014 m, respectively.

TABLE 5. Peak values ($z = 0.015$ m).

H (m)	Axial component (Gauss)	Radial component (Gauss)
0.009	732.492	339.489
0.0128	2511.898	1533.278
0.013	2643.609	1662.626
0.014	3334.499	2655.404

TABLE 6. Peak values ($z = -0.0022$ m).

H (m)	Axial component (Gauss)	Radial component (Gauss)
0.009	1614.481	632.498
0.0128	1847.806	697.455
0.013	1857.445	699.840
0.014	1902.687	711.545

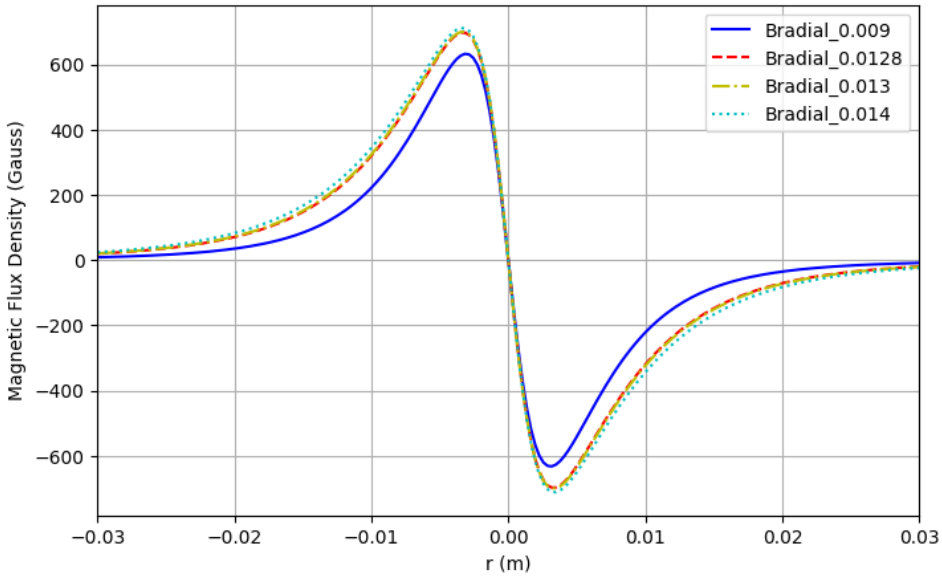

FIGURE 11. Magnetic field distribution according to various heights H: Radial component. Parameters of the permanent magnet and coordinates of measuring points are $J = 1$ Tesla, $a = 0.3$, $z = -0.0022$ m, $r = [-0.03\,\text{m}, 0.03\,\text{m}]$. Bradial_0.009, Bradial_0.0128, Bradial_0.013, Bradial_0.014 — Magnetic flux density with the height H equal to 0.009 m, 0.0128 m, 0.013 m, and 0.014 m, respectively.

of the field increase from 1614.481 Gauss to 1902.687 Gauss with the increase of the height from 0.009 m to 0.014 m, respectively. On the other hand, the radial component decreases to zero at the revolute axis and gradually increases to reach maximum when the radial distance increases before nonlinearly decreasing. The maximum magnitudes increase from 632.498 Gauss to 711.545 Gauss with the increase of the height from 0.009 m to 0.014 m. The maximum magnitudes increase from 632.498 Gauss to 711.545 Gauss with the increase of the height from 0.009 m to 0.014 m (Table 6).

5. DISCUSSION AND CONCLUSION

Due to the capability of producing a permanent magnetic field, permanent magnets have been found in many applications. Based on algebraic and geometrical manipulation, fast-computed expressions of the axial and radial components of the magnetic field generated by a magnetised paraboloid are derived while the azimuthal component is equal to zero. It is demonstrated that the semi-analytical models are in good agreement with the Finite Element Method while they are multiple magnitudes faster in terms of computational time. Analysing the field distribution, it is shown that the axial component is concentrated around the revolute axis, and it is pointier on the side close to the apex than the side close to the base of the paraboloid. This pattern can be useful to applications such as medical interference where the magnetic field concentration is needed to avoid the negative effect of the magnetic field on unaffected areas, e.g., transcranial static magnetic field stimulation [4–6]. On the other hand, the magnetic field decreases to zero at the revolute axis for the radial component. This component then increases to reach a maximum before decreasing nonlinearly. Moreover, the maximum magnitudes of the field components decrease with the increase of the coefficient and increase with the increase of the height H. The fast-computed field models and understanding of the field distribution are expected to facilitate the design and optimization process of magnetic devices.

REFERENCES

[1] Coey, J. M. D., "Permanent magnet applications," *Journal of Magnetism and Magnetic Materials*, Vol. 248, No. 3, 441–456, 2002.

[2] Furlani, E. P., *Permanent Magnet and Electromechanical Devices: Materials, Analysis, and Applications*, Academic Press, 2001.

[3] Carneiro, P., M. P. S. Dos Santos, A. Rodrigues, J. A. F. Ferreira, J. A. O. Simões, A. T. Marques, and A. L. Kholkin, "Electromagnetic energy harvesting using magnetic levitation architectures: A review," *Applied Energy*, Vol. 260, 114191, 2020.

[4] Dileone, M., L. Mordillo-Mateos, A. Oliviero, and G. Foffani, "Long-lasting effects of transcranial static magnetic field stimulation on motor cortex excitability," *Brain Stimulation*, Vol. 11, No. 4, 676–688, 2018.

[5] Oliviero, A., L. Mordillo-Mateos, P. Arias, I. Panyavin, G. Foffani, and J. Aguilar, "Transcranial static magnetic field stimulation of the human motor cortex," *The Journal of Physiology*, Vol. 589, No. 20, 4949–4958, 2011.

[6] Shimomura, R., S. Shibata, S. Koganemaru, M. Minakuchi, S. Ichimura, A. Itoh, K. Shimotake, and T. Mima, "Transcranial static magnetic field stimulation (tSMS) can induce functional recovery in patients with subacute stroke," *Brain Stimulation: Basic, Translational, and Clinical Research in Neuromodulation*, Vol. 16, No. 3, 933–935, 2023.

[7] Hart, S., K. Hart, and J. P. Selvaggi, "Analytical expressions for the magnetic field from axially magnetized and conically shaped permanent magnets," *IEEE Transactions on Magnetics*, Vol. 56, No. 7, 1–9, 2020.

[8] Nguyen, V. T. and T.-F. Lu, "Analytical expression of the magnetic field created by a permanent magnet with diametrical magnetization," *Progress In Electromagnetics Research C*, Vol. 87, 163–174, 2018.

[9] Nguyen, V. T. and T.-F. Lu, "Modelling of magnetic field distributions of elliptical cylinder permanent magnets with diametrical magnetization," *Journal of Magnetism and Magnetic Materials*, Vol. 491, 165569, 2019.

[10] Tejedor, M., H. Rubio, L. Elbaile, and R. Iglesias, "External fields created by uniformly magnetized ellipsoids and spheroids," *IEEE Transactions on Magnetics*, Vol. 31, No. 1, 830–836, 1995.

[11] Yan, L., I.-M. Chen, G. Yang, and K.-M. Lee, "Analytical and experimental investigation on the magnetic field and torque of a permanent magnet spherical actuator," *IEEE/ASME Transactions on Mechatronics*, Vol. 11, No. 4, 409–419, 2006.

[12] Park, J., C. Lee, S. Lee, and C.-H. Im, "Comparison of magnetic field distributions generated by various permanent magnets for transcranial static magnetic stimulation: A simulation study," *Computers in Biology and Medicine*, Vol. 114, 103476, 2019.

[13] Van Rossum, G., *et al.*, "Python programming language," in *USENIX Annual Technical Conference*, Vol. 41, No. 1, 1–36, 2007.

[14] Padmanabhan, T. R., *Programming with Python*, Springer, 2016.

[15] Fangohr, H., "A comparison of C, MATLAB, and Python as teaching languages in engineering," in *Computational Science — ICCS 2004: 4th International Conference, Kraków, Poland, June 6-9, 2004, Proceedings, Part IV 4*, 1210–1217, 2004.

[16] Dale, N. B. and C. Weems, *Programming and Problem Solving with C++*, Jones & Bartlett Publishers, 2014.

[17] Zaccone, G., *Python Parallel Programming Cookbook*, Packt Publishing Ltd, 2015.